Plasma Phys. Control. Fusion 63 (2021) 125032 (15pp)

https://doi.org/10.1088/1361-6587/ac318d

Electron acceleration using twisted laser wavefronts

Yin Shi^{1,2,*}, David R Blackman² and Alexey Arefiev^{2,*}

E-mail: shiyin@ustc.edu.cn and aarefiev@eng.ucsd.edu

Received 16 July 2021, revised 28 September 2021 Accepted for publication 20 October 2021 Published 15 November 2021



Abstract

Using plasma mirror injection we demonstrate, both analytically and numerically, that a circularly polarized helical laser pulse can accelerate highly collimated dense bunches of electrons to several hundred MeV using currently available laser systems. The circular-polarized helical (Laguerre-Gaussian) beam has a unique field structure where the transverse fields have helix-like wave-fronts which tend to zero on-axis where, at focus, there are large on-axis longitudinal magnetic and electric fields. The acceleration of electrons by this type of laser pulse is analyzed as a function of radial mode number and it is shown that the radial mode number has a profound effect on electron acceleration close to the laser axis. Using three-dimensional particle-in-cell simulations a circular-polarized helical laser beam with power of 0.6 PW is shown to produce several dense attosecond bunches. The bunch nearest the peak of the laser envelope has an energy of 0.47 GeV with spread as narrow as 10%, a charge of 26 pC with duration of ~400 as, and a very low divergence of 20 mrad. The confinement by longitudinal magnetic fields in the near-axis region allows the longitudinal electric fields to accelerate the electrons over a long period after the initial reflection. Both the longitudinal E and B fields are shown to be essential for electron acceleration in this scheme. This opens up new paths toward attosecond electron beams, or attosecond radiation, at many laser facilities around the world.

Keywords: particle-in-cell simulation, laser driven electron acceleration, high intensity laser-plasma interactions, twisted laser

(Some figures may appear in colour only in the online journal)

1. Introduction

Laser-driven electron accelerators have become a very active area of research due to technological developments and improvements of high-power laser beams [1]. There are usually two common approaches. One approach is laser wake-field acceleration [2] that utilizes plasma electric fields whose strength is related to the plasma density. Another approach is direct laser acceleration [3] that relies on the fields of the laser for the energy transfer inside a plasma (e.g. see [4])

or in vacuum [5]. In the vacuum regime, transverse electron expulsion typically terminates the energy gain and leads to strong electron divergence. This is the reason why direct laser acceleration in vacuum has been deemed ineffective and most of the research has been focused on the plasma regime where collective fields prevent the expulsion [6–8]. In an attempt to mitigate the expulsion in the vacuum regime, some studies examined alternative approaches utilizing longitudinal electric fields of a radially polarized beam [9] and higher-order Gaussian beams [10] for electron acceleration.

Currently there are several multi-PW laser systems operational in the world, with several more due to come online in the next few years [1]. The biggest of the new systems

¹ Department of Plasma Physics and Fusion Engineering, University of Science and Technology of China, Hefei 230026, People's Republic of China

² Department of Mechanical and Aerospace Engineering, University of California at San Diego, La Jolla, CA 92093, United States of America

^{*} Authors to whom any correspondence should be addressed.

recently proposed, at the Shanghai Superintense-Ultrafast Laser Facility [11], is pushing the 100 PW limit and will be in development over the next decade. At the same time, new optical techniques using helical wave-fronts [12, 13] are being developed. One of the key advantages of the helical, or Laguerre-Gaussian, laser mode is that it can be produced, at high efficiency, from a standard Gaussian laser pulse in reflection from a fan-like structure [13, 14]. Very significant differences can be seen when comparing the laserplasma interactions of conventional laser beams to those of helical beams, some of which have been examined in simulations [14–23], and some have begun to be explored in recent experiments [12, 24-27]. An electron acceleration scheme has recently been proposed where a high-power high-intensity circular-polarized Laguerre-Gaussian beam is reflected from a plasma mirror [28]. The unique field structure of this beam both confines and accelerates tightly packed electron bunches to GeV energies with a narrow energy spread.

In this article, we show using 3D particle-in-cell (PIC) simulations that the same electron acceleration scheme can be successfully applied (1) using significantly lower laser power than that used in [28] and (2) using oblique incidence. Specifically, we show that a 600 TW laser beam generates several dense attosecond bunches at intervals similar to the laser wavelength. The bunch nearest the peak of the laser envelope gains an energy of 0.47 GeV (10% FWHM energy spread), while maintaining a bunch charge as high as 26 pC. The tightly confined bunch has a duration of \sim 400 as and a remarkably low divergence of just 1.15° (20 mrad). In addition to this, the scheme is demonstrated to be tenable with an angle of incidence as high as 25°. Our results show that the electron acceleration by helical beams is not limited to high-power high-intensity lasers and can be successfully explored at a wide range of laser facilities.

The rest of this paper is organized as follows. Section 2 examines the field structure of linearly and circularly polarized laser beams with twisted wavefronts. The near-axis structure of the longitudinal electric field for different radial modes is explicitly derived. Section 3 is dedicated to estimating the acceleration that the longitudinal fields can provide and the effect of the radial mode structure of the laser on this acceleration. In section 4, we present results of a 3D PIC simulation for a 600 TW laser beam with twisted wavefronts whose near-axis field structure is dominated by longitudinal electric and magnetic fields. Section 5 is concerned with exploring the role of the longitudinal magnetic field where the effect of this field on the bunch density and particle trajectories is shown, including the possible reliability of this model with an oblique angle of incidence. In section 6, we summarize the main results of this work.

2. Field topology of a laser beam with twisted wavefronts

In this section, we examine the field topology of linearly and circularly polarized laser beams with twisted wavefronts. We show that, for a properly chosen twist index, the field structure in the region close to the axis of the beam can primarily consist of longitudinal electric and magnetic fields. The differences between radial modes are explicitly emphasized.

2.1. Linearly polarized beam

We start by considering a linearly polarized laser beam with wavelength λ_0 propagating in vacuum along the x-axis. We assume that the diffraction angle, defined as $\theta_d = w_0/x_R$, is small, where w_0 is the beam waist, and $x_R = \pi w_0^2/\lambda_0$ is the Rayleigh range. Without any loss of generality, we assume that the laser electric field is polarized along the y-axis. In this case, it is convenient to describe the field structure using a vector potential A that satisfies the Lorenz gauge condition and has only one non-zero component, A_y . The paraxial wave equation for A_y has the form

$$\left[\frac{\partial^2}{\partial \widetilde{y}^2} + \frac{\partial^2}{\partial \widetilde{z}^2} + 4i\frac{\partial}{\partial \widetilde{x}}\right] A_y = 0, \tag{1}$$

where, for compactness, the longitudinal coordinate x is normalized to x_R and the transverse coordinates y and z are normalized to w_0 :

$$\widetilde{x} = x/x_R,$$
 (2)

$$\widetilde{y} = y/w_0, \tag{3}$$

$$\widetilde{z} = z/w_0. \tag{4}$$

Equation (1) implies the following form of the solution with $\omega = 2 \pi c / \lambda_0$:

$$A_{v} = \Psi_{v}(\widetilde{x}, \widetilde{y}, \widetilde{z})g(\xi)\exp(i\xi), \tag{5}$$

where g is the envelope function with max(g) = 1 and

$$\xi \equiv 2\widetilde{x}/\theta_d^2 - \omega t \tag{6}$$

is the phase variable.

The transverse electric field in the paraxial approximation, i.e. at $\theta_d \ll 1$, is given by

$$E_{y} \approx -\frac{1}{c} \frac{\partial A_{y}}{\partial t} = \frac{i\omega}{c} A_{y}.$$
 (7)

We are interested in solutions of the form

$$E_{v} = E_{0}g(\xi) \exp(i\xi) \psi_{l,p}(\widetilde{x}, \widetilde{r}, \phi)$$
 (8)

where

$$\psi_{p,l}(\widetilde{x},\widetilde{r},\phi) = C_{p,l}f(\widetilde{x})^{|l|+1+2p} (1+\widetilde{x}^2)^p L_p^{|l|} \left(\frac{2\widetilde{r}^2}{1+\widetilde{x}^2}\right) \left(\sqrt{2}\widetilde{r}\right)^{|l|} \times \exp\left[-\widetilde{r}^2 f(\widetilde{x})\right] \exp\left(il\phi\right) \tag{9}$$

is a mode with a twist index l and radial index p. Here we introduced

$$\widetilde{r} = \sqrt{\widetilde{y}^2 + \widetilde{z}^2}, \quad \phi = \arctan(\widetilde{z}/\widetilde{y}), \quad f(\widetilde{x}) = \frac{1 - i\widetilde{x}}{1 + \widetilde{x}^2}.$$
 (10)

The $L_p^{|l|}$ function is the generalized Laguerre polynomial and $C_{p,l}$ is a normalization constant. The modes $\psi_{p,l}(\widetilde{x},\widetilde{r},\phi)$ are orthonormal at a given \widetilde{x} [29], with

$$C_{p,l} = \sqrt{\frac{2p!}{\pi(p+|l|)!}},$$
 (11)

such that

$$\int_{0}^{2\pi} d\phi \int_{0}^{\infty} \psi_{p,l}(\widetilde{x},\widetilde{r},\phi) \psi_{p,l}^{*}(\widetilde{x},\widetilde{r},\phi) \widetilde{r} d\widetilde{r} = 1.$$
 (12)

It is worth pointing out that E_0 in equation (8) is not the peak amplitude of E_v . It is therefore convenient to introduce

$$E_0^* \equiv \sqrt{\frac{2}{\pi}} E_0, \tag{13}$$

which is the peak amplitude of the transverse electric field in the beam with l = 0.

The transverse magnetic field has a *z*-component only, since $\mathbf{B} = \nabla \times \mathbf{A}$. In the paraxial approximation, we have

$$B_z = \frac{1}{x_R} \frac{\partial A_y}{\partial \widetilde{x}} \approx \frac{2i}{\theta_d w_0} A_y. \tag{14}$$

After taking into account that $\theta_d = \lambda_0/\pi w_0$, we find that $B_z = E_y$. The longitudinal component of the Poynting vector S is then given by $S_x = (c/4 \pi) (\text{Re}E_y)^2$ and the peak period-averaged power for the linearly polarized beam is

$$P_{lin} = \left\langle \int_{0}^{2\pi} d\phi \int_{0}^{\infty} S_{x} r dr \right\rangle$$

$$= \frac{cw_{0}^{2}}{4\pi} \int_{0}^{2\pi} d\phi \int_{0}^{\infty} \left\langle (\text{Re}E_{y})^{2} \right\rangle \widetilde{r} d\widetilde{r}, \qquad (15)$$

where the angle brackets indicate the time-averaging. It is convenient to compute the power in the focal plane, i.e. at $\tilde{x} = 0$. We use the expression given by equation (8) to find that

$$P_{lin} = \frac{cw_0^2}{8\pi} E_0^2 = \frac{\pi}{2} \frac{a_0^2 w_0^2 m_e^2 c^5}{\lambda_0^2 e^2},$$
 (16)

where

$$a_0 = |e|E_0/m_e c\omega \tag{17}$$

is a dimensionless parameter, and e and m_e are the electron charge and mass. We have explicitly taken into account the normalization condition given by equation (12). The advantage of the chosen normalization is that the power P is the same for different modes with the same E_0 or a_0 .

The longitudinal laser electric and magnetic fields can be calculated from the $(\nabla \cdot \mathbf{E}) = 0$ and $(\nabla \cdot \mathbf{B}) = 0$ conditions, respectively. In the paraxial approximation, we have

$$E_x \approx \frac{i\theta_d}{2} \frac{\partial E_y}{\partial \widetilde{y}}, \qquad B_x \approx \frac{i\theta_d}{2} \frac{\partial E_y}{\partial \widetilde{z}}.$$
 (18)

It follows from equations (8)–(10) that

$$E_{x}^{\pm} = \begin{cases} \frac{i\theta_{d}}{2} \left[\frac{|l|}{\widetilde{r}} e^{\mp i\phi} - 2f \, \widetilde{r} \cos \phi - \frac{2}{1 + \widetilde{x}^{2}} \frac{L_{p-1}^{|l|+1}}{L_{p}^{|l|}} \cos \phi \right] E_{y}; \text{ for } p \geq 1, \\ \frac{i\theta_{d}}{2} \left[\frac{|l|}{\widetilde{r}} e^{\mp i\phi} - 2f \, \widetilde{r} \cos \phi \right] E_{y}; \text{ for } p = 0, \end{cases}$$

$$(19)$$

$$B_{x}^{\pm} = \begin{cases} \frac{\theta_{d}}{2} \left[\mp \frac{|l|}{\widetilde{r}} e^{\mp i\phi} - 2if \, \widetilde{r} \sin \phi - \frac{2i}{1 + \widetilde{x}^{2}} \frac{L_{p-1}^{|l|+1}}{L_{p}^{|l|}} \sin \phi \right] E_{y}; \text{ for } p \ge 1, \\ \frac{\theta_{d}}{2} \left[\mp \frac{|l|}{\widetilde{r}} e^{\mp i\phi} - 2if \, \widetilde{r} \sin \phi \right] E_{y}; \text{ for } p = 0, \end{cases}$$

$$(20)$$

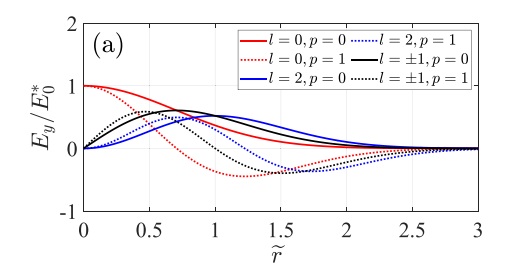
where the superscript on the left-hand side represents the sign of l.

The twist of the field represented by l qualitatively changes the topology of the transverse and longitudinal fields. We are particularly interested in the field structure close to the central axis, i.e. at $\widetilde{r} \to 0$. It is important to distinguish three cases based on the value of the twist index: l=0, |l|=1, and |l|>1. In the near-axis region, we have $E_y \propto \widetilde{r}^{|l|} \exp(il\phi)$. In the case of l=0 or a beam without a twist, the longitudinal fields vanish on the central axis, while the transverse fields reach their maximum value. In the case of |l|>1, all laser fields vanish on the central axis. The most unusual is the case of |l|=1,

because in this case the longitudinal rather than transverse fields peak on axis. As a result, the near-axis field structure is dominated by longitudinal fields. Note that according to equations (19) and (20) these fields are not axis-symmetric.

2.2. Circularly polarized beam

The results of the previous subsection can be readily generalized to the case of a circularly polarized laser pulse. In addition to E_y , the laser beam also has an E_z -component. We set $E_z = i\sigma E_y$, where $\sigma = 1$ corresponds to the right-circularly polarized



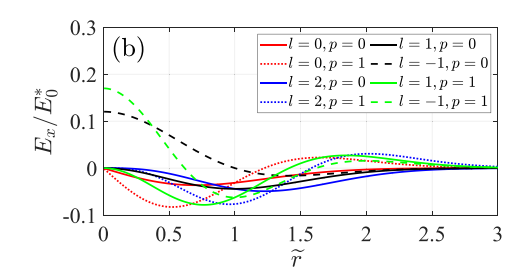


Figure 1. Transverse and longitudinal electric field structure in the focal plane, $\tilde{x} = 0$, of right-circularly polarized beams ($\sigma = 1$) with $l = 0, \pm 1, 2$ and p = 0, 1. All beams have the same E_0 and the same diffraction angle, $\theta_d = 8.5 \times 10^{-2}$. The fields are normalized to E_0^* , which is the peak amplitude of the transverse electric field in the beam with l = 0.

wave and $\sigma=-1$ corresponds to the left-circularly polarized wave. The longitudinal electric and magnetic fields can again be calculated using the $(\nabla \cdot \boldsymbol{E})=0$ and $(\nabla \cdot \boldsymbol{B})=0$ equations, respectively. In the paraxial approximation, we have

$$E_x \approx \frac{i\theta_d}{2} \left(\frac{\partial E_y}{\partial \widetilde{y}} + \frac{\partial E_z}{\partial \widetilde{z}} \right),$$
 (21)

$$B_x \approx \frac{i\theta_d}{2} \left(\frac{\partial E_y}{\partial \tilde{z}} - \frac{\partial E_z}{\partial \tilde{y}} \right).$$
 (22)

After substituting $E_z = i\sigma E_y$ into these equations, we find that

$$E_{x}^{\pm} = \begin{cases} i\theta_{d}E_{y} \left[\frac{|l|}{\widetilde{r}} \frac{1 \mp \sigma}{2} e^{\mp i\phi} - \widetilde{r}fe^{i\sigma\phi} - \frac{1}{1 + \widetilde{x}^{2}} \frac{L_{p-1}^{|l|+1}}{L_{p}^{|l|}} e^{i\sigma\phi} \right]; p \geq 1, \\ i\theta_{d}E_{y} \left[\frac{|l|}{\widetilde{r}} \frac{1 \mp \sigma}{2} e^{\mp i\phi} - \widetilde{r}fe^{i\sigma\phi} \right]; p = 0, \end{cases}$$

$$(23)$$

$$B_{x}^{\pm} = \begin{cases} \theta_{d} E_{y} \left[\frac{|l|}{\widetilde{r}} \frac{\sigma \mp 1}{2} e^{\mp i\phi} - \widetilde{r} f \sigma e^{i\sigma\phi} - \frac{\sigma}{1 + \widetilde{x}^{2}} \frac{L_{p-1}^{|l|+1}}{L_{p}^{|l|}} e^{i\sigma\phi} \right]; p \ge 1, \\ \theta_{d} E_{y} \left[\frac{|l|}{\widetilde{r}} \frac{\sigma \mp 1}{2} e^{\mp i\phi} - \widetilde{r} f \sigma e^{i\sigma\phi} \right]; p = 0, \end{cases}$$

$$(24)$$

where the superscripts on the left-hand side again represent the sign of l.

Only for |l|=1 the longitudinal rather than transverse fields peak on axis. However, the two circular polarizations (right and left) are not equivalent. In the case of $\sigma=-l$, the longitudinal fields reach their highest amplitude at $\widetilde{r}\to 0$. On the other hand, in the case of $\sigma=l$, the longitudinal fields vanishes on axis. The transverse fields vanish on axis in both cases. It is worth pointing out that, in contrast to the linearly polarized beam, the longitudinal fields of the circularly polarized beam with $\sigma=-l$ are axis-symmetric.

Figure 1 shows the field structure for right-circularly polarized beams ($\sigma=1$) with different values of the twist index l and radial index p. In agreement with our analysis, the transverse field in figure 1(a) only peaks on axis for the beams without a twist (l=0). In all other cases, the transverse field vanishes at $\widetilde{r} \to 0$. The longitudinal field, shown in figure 1(b), only peaks on axis for the beam with l=-1. As predicted, the longitudinal field vanishes at $\widetilde{r} \to 0$ for l=1.

It must be pointed out that the circularly polarized beams with |l| = 1 have two, rather than one, rotations to consider:

the rotation of the electric field maxima about the central axis due to the wavefronts twist and the rotation of the electric field vector due to the choice of polarization. In the case with |l|=1 and $\sigma=-l$, the rotation of the transverse electric field vector due to the polarization and the twist of the transverse field wavefronts have opposing chiralities. Figure 2 (bottom row) provides schematic diagrams showing the two rotations. For comparison, the upper row in figure 2 shows the field topology for a linearly polarized beam, with $E_{\perp}=E_y$. Recall that the circularly polarized beam is a superposition of two linearly polarized beams.

In the sections that follow, we focus on electron acceleration in the near-axis region by E_x of a circularly polarized laser beam with l=-1 and $\sigma=1$. In order to obtain a compact expression for E_x , we set $\tilde{r}=0$ in equation (23) and substitute the expression for E_y given by equation (8), which yields

$$E_{x}(\widetilde{r}=0) = iE_{\parallel}^{\max} f^{2(1+p)} (1+\widetilde{x}^{2})^{p} g(\xi) e^{i\xi} = \frac{ig(\xi) E_{\parallel}^{\max}}{1+\widetilde{x}^{2}}$$

$$\times \exp\left[i\xi - i2(1+p) \tan^{-1}\widetilde{x}\right], \qquad (25)$$

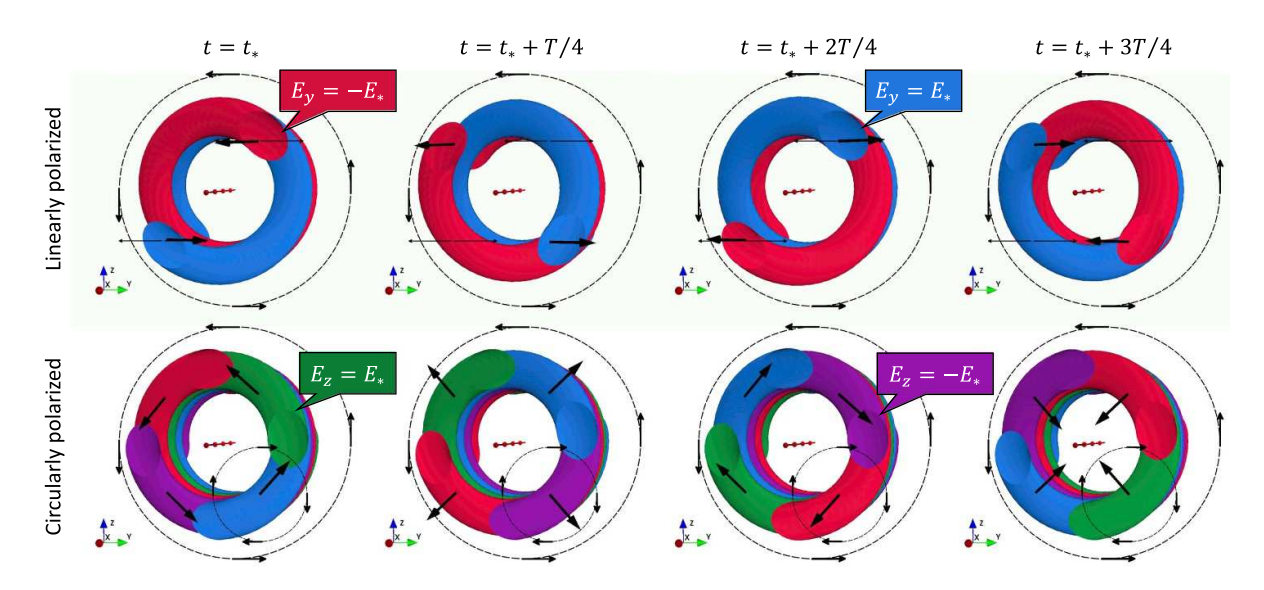


Figure 2. Schematic representation of the transverse electric field topology for a linearly polarized beam (top row) with l=-1 and p=0 and a circularly polarized beam (bottom row) with l=-1, p=0, and $\sigma=-l$. The diagrams show one wavelength near the focal plane of each beam. The color-coded surfaces are the surfaces of the constant amplitude $|E_{\perp}| = E_*$: blue is positive E_y , red is negative E_y , green is positive E_z , and purple is negative E_z . The large arrows show the direction of E_{\perp} at a given location. The small black arrows placed on the large circles represent the motion of $|E_{\perp}|$ peaks over time. The small black arrows placed on the small circles in the bottom row represent the direction of rotation of the electric field over time. The red structure at the center of each image represents the the central axis of each beam. The images from left to right are at times incremented by a quarter period T/4, where T=2 π/ω .

where

$$E_{\parallel}^{\text{max}} = 2\sqrt{\frac{p+1}{\pi}}\theta_d E_0 = \frac{2}{\pi}\sqrt{\frac{p+1}{\pi}}\frac{\lambda_0}{w_0}E_0$$
 (26)

is the peak value of the longitudinal electric field. A feature that is important for electron acceleration is the explicit dependence of the phase on p. This will be discussed in more detail in section 3. The peak period-averaged power P for the circularly-polarized beam is twice the power P_{lin} for a single linearly polarized beam with the same amplitude E_0 . Taking this into account and using the expression for P_{lin} given by equation (16), we obtain the following expression for P in terms of the amplitude of the longitudinal field:

$$P = \frac{\pi^4}{4(p+1)} \frac{w_0^4}{\lambda_0^4} \frac{m_e^2 c^5}{e^2} a_{\parallel}^2, \tag{27}$$

where $a_{\parallel} \equiv |e|E_{\parallel}^{\rm max}/m_e c\omega$. Equation (27) can be recast as an expression for normalized amplitudes of longitudinal electric and magnetic fields for a given power P in the laser beam:

$$a_{\parallel} \equiv \frac{|e|E_{\parallel}^{\text{max}}}{m_e c \omega} = \frac{|e|B_{\parallel}^{\text{max}}}{m_e c \omega} \approx 71 \sqrt{p+1} \left(\frac{\lambda_0}{w_0}\right)^2 P^{1/2} [\text{PW}]. \tag{28}$$

We conclude this section by pointing out that the longitudinal fields can be strong even for $\theta_d \ll 1$. Let us take a P=0.6 PW circularly-polarized beam with l=-1, $\sigma=1$, and p=0. The focal spot size is $w_0=3.0$ μ m and the wavelength is $\lambda_0=0.8$ μ m. In this case, $\theta_d\approx 8.5\times 10^{-2}$, so our analysis that was performed in the paraxial approximation is applicable to this beam. It follows from equation (26) that $E_{\parallel}^{\rm max}\approx 0.1E_0$.

Taking into account that $E_y^{\rm max}=E_0~C_{0,l}|l|^{|l|/2}\exp{(-|l|/2)}$ for p=0, we find that $E_{\parallel}^{\rm max}/E_y^{\rm max}=B_{\parallel}^{\rm max}/B_y^{\rm max}\approx 0.2$. We also find from equation (28) that $a_{\parallel}\approx 3.8$. The corresponding dimensional field amplitudes are $E_{\parallel}^{\rm max}\approx 1.5~\times 10^{13}~{\rm V~m^{-1}}$ and $B_{\parallel}^{\rm max}\approx 51~{\rm kT}$.

3. Preliminary estimates for electron acceleration

In this section, we perform preliminary estimates for electrons accelerated in the near-axis region by a helical laser beam whose field structure in this region predominantly consists of longitudinal electric and magnetic fields. We assume that the electrons are injected into the laser beam near the focal plane located at $\tilde{x} = 0$. The injection is implied to occur when an incident beam is reflected off a mirror at normal incidence. This process is examined self-consistently in section 4 and section 5 using kinetic simulations.

The phase velocity, v_{ph} , of E_{\parallel} wavefronts plays a key role in electron acceleration along the central axis. For simplicity, we limit our analysis to the part of the pulse that is near the peak of the envelope, which means that we can set $g(\xi) \approx 1$ in equation (25). In order to determine v_{ph} , it is convenient to re-write the expression for the longitudinal electric field given by equation (25) as

$$E_{\parallel} = -\frac{E_{\parallel}^{\text{max}} \sin(\Phi + \Phi_0)}{1 + x^2 / x_B^2},$$
 (29)

where the phase Φ is given by

$$\Phi = 2 \left[\theta_d^{-2}(x/x_R) - (p+1) \tan^{-1}(x/x_R) \right] - \omega t.$$
 (30)

The constant Φ_0 can be interpreted as the injection phase for an electron that starts its acceleration at $x \approx 0$ at $t \approx 0$. We define the phase velocity as $v_{ph} = dx/dt$ for $\Phi = \text{const.}$ We differentiate equation (30), where $\Phi = \text{const.}$ to obtain

$$0 = \frac{v_{ph}}{c} - \frac{v_{ph}}{c} \frac{(p+1)\theta_d^2}{1 + x^2/x_P^2} - 1,$$
 (31)

where it was taken into account that $\theta_d^2 = \lambda_0/\pi x_R$. In the paraxial approximation ($\theta_d \ll 1$), the second term on the right-hand side is small. We neglect this term to find that $v_{ph}/c \approx 1$. In order to find the correction associated with θ_d , we set $v_{ph}/c = 1$ in the second term on the right-hand side of equation (31) and obtain the following expression for the relative degree of superluminosity along the central axis:

$$\frac{v_{ph} - c}{c} \approx \frac{(p+1)\theta_d^2}{1 + x^2/x_p^2}.$$
 (32)

The key feature here is the explicit dependence on the radial index p, with the superluminosity being higher for higher-order radial modes.

The electron unavoidably slips with respect to the wavefronts as it moves forward, which limits its energy gain. The slipping is determined by the difference $v_{ph} - v_x$, where $v_{ph} \ge c$ and $v_x < c$. As the electron becomes ultra-relativistic due to the acceleration by E_{\parallel} , it enters a regime where $c - v_x \ll v_{ph} - c$. In this regime, the slipping, or dephasing, is primarily determined by the relative degree of superluminosity given by equation (32). The lowest estimate for the phase slip experienced by an electron that has traveled from x_0 to x is obtained by setting $x = x_0 + c(t - t_0)$ in equation (30), which yields

$$\Delta \Phi = 2(p+1) \left[\tan^{-1}(x_0/x_R) - \tan^{-1}(x/x_R) \right]. \tag{33}$$

For $x_0 \ll x_R$, this expression reduces to $\Delta \Phi = -2(p+1)\tan^{-1}(x/x_R)$. The phase velocity is superluminal near x=0, but it decreases to c at $x\gg x_R$. As a result, the total phase slip is finite and it approaches $\Delta \Phi = -(p+1)\pi$ at $x\gg x_R$. There is a significant difference between the p=0 mode and higher order radial modes. At p=0, the phase slip is $\Delta \Phi = -\pi$, which means that some electrons (this depends on the initial phase) can remain in the accelerating phase of E_{\parallel} until the laser defocuses $(x\gg x_R)$ and E_{\parallel} becomes very weak. In contrast to that, all electrons experience deceleration by E_{\parallel} at $p\geq 1$, because they slip into the decelerating phase prior to strong defocusing at $x\gg x_R$.

In order to estimate the electron energy gain from E_{\parallel} , we assume that the electron is ultra-relativistic with $c-v_x\ll v_{ph}-c$. In this case, the phase Φ in equation (29) can be replaced by $\Phi\approx\Phi_0+\Delta\Phi$, where $\Delta\Phi$ is given by the already derived equation (33). The change in electron momentum during the acceleration is obtained by integrating the momentum balance equation $dp_{\parallel}/dt=-|e|E_{\parallel}$, which yields

$$\Delta p_{\parallel} = |e|E_{\parallel}^{\text{max}} \int_{t_0}^{t} \frac{\sin(\Delta \Phi + \Phi_0 + \pi)dt'}{1 + (x')^2/x_R^2},$$
 (34)

where x' is the electron location at time t'. We note that $dx'/dt' \approx c$ in the considered regime, so we can switch from

integration over time to integration over the longitudinal coordinate by replacing dt' with dx'/c. After substituting the expression for equation (33), we obtain

$$\Delta p_{\parallel} = \frac{|e|E_{\parallel}^{\text{max}}}{c} \int_{x_0}^{x} \frac{\sin(\Delta \Phi + \Phi_0) dx'}{1 + (x')^2 / x_R^2}$$

$$= -\frac{|e|E_{\parallel}^{\text{max}} x_R}{2(p+1)c} \left(\cos \Phi_0 - \cos\left[\Phi_0 + 2(p+1)\tan^{-1}(x_0/x_R)\right] - 2(p+1)\tan^{-1}(x/x_R)\right]. \tag{35}$$

This result can be further simplified by assuming that $x_0 \ll x_R$, so that $\tan^{-1}(x_0/x_R) \approx 0$ and

$$\Delta p_{\parallel} = -\frac{|e|E_{\parallel}^{\text{max}}x_R}{2(p+1)c} \left(\cos\Phi_0 - \cos\left[\Phi_0 - 2(p+1)\tan^{-1}(x/x_R)\right]\right). \tag{36}$$

Equation (36) represents an important qualitative result, as it shows that the electrons can retain a significant portion of the energy they gain from E_{\parallel} . We find the terminal momentum gain by taking the limit of $x/x_R \to \infty$ in equation (36). There is a profound difference between odd and even radial radial modes, i.e. odd and even radial indices p. In the case of even modes with (e.g. p = 0, 2, 4), we have

$$\Delta p_{\parallel}^{term} = \frac{|e|E_{\parallel}^{\text{max}} x_R}{(p+1)c} \cos(\Phi_0 - \pi). \tag{37}$$

The energy gain occurs for $0.5\pi < \Phi_0 < 1.5\pi$ regardless of the radial mode structure. Our assumption that the electron is moving forward with an ultra-relativistic velocity breaks down for $1.5\pi/<\Phi_0<2.5\pi$, which invalidates equation (37) for these injection phases. In contrast to the even radial modes, there is no terminal momentum gain, $\Delta p_{\parallel}^{term}=0$, for the odd radial modes regardless of the injection phase. It is worth pointing out that this estimate was obtained under the assumption that the electron is ultra-relativistic, so the analysis has to be revised along the parts of the trajectory where $c-v_x \geq v_{ph}-c$. However, the value of $\Delta p_{\parallel}^{term}$ is unlikely to increase dramatically as a result.

Figure 3 illustrates the results of our analysis for three different radial modes, p = 0, 1, and 2. The solid curves show electron acceleration by a beam with p = 0, as predicted by equation (36). Both electrons are injected at a phase that leads to a net momentum gain. However, the delayed injection of the electron shown with the solid blue curve ($\Phi_0 = 0.6\pi$) means that it slips into the decelerating phase before the amplitude of E_{\parallel} becomes negligibly small due to the beam diffraction. As a result, the net momentum gain is two times lower than for the case of $\Phi_0 = 0.9\pi$. Higher-order modes speed up the electron slip into the decelerating phase, because the relative degree of superluminosity given by equation (32) increases with p. This trend is clearly shown by the dashed curves, representing modes with p = 1 and p = 2, respectively. In both cases, the injection phase is $\Phi_0 = 0.9\pi$, which is the same phase as that for the solid red curve (p = 0). The green dashed curve, corresponding to p = 1, rolls over, after a peak in momentum

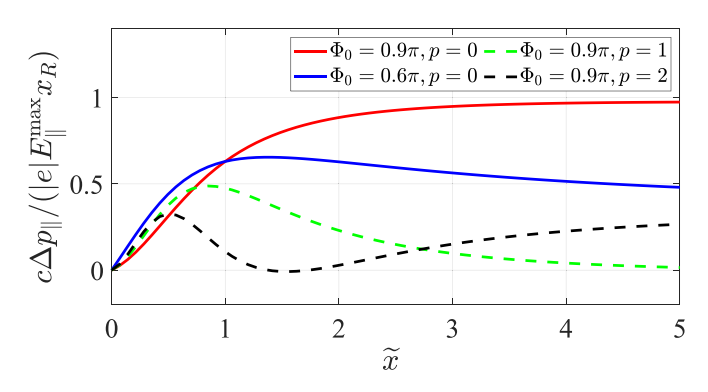


Figure 3. The momentum gain predicted by equation (36) for electrons injected at phase Φ_0 into a right-circularly polarized beam $(\sigma=1,l=-1)$. The solid curves are for a beam with the radial index p=0, whereas the green and black dashed curves correspond to beams with p=1 and p=2, respectively.

gain, at $\widetilde{x}\approx 1$, whereas the black dashed curve, corresponding to p=2, rolls over even sooner when the electron reaches $\widetilde{x}\approx 0.5$. In the case of p=1, the electron remains in the decelerating phase until the beam experiences significant diffraction. As a result, there is no net momentum gain. In the case of p=2, the dephasing is faster, so the electron enters another accelerating region of the beam when it reaches $\widetilde{x}\approx 1.5$. The acceleration continues until the diffraction eliminates E_{\parallel} . In this case there is a net momentum gain, but it is smaller than in the case of p=0 because the acceleration time is shorter and the accelerating field (due to the diffraction) is weaker.

It is useful to recast our results for the momentum gain in terms of electron energy. The energy of an ultra-relativistic electrons with momentum ${\bf p}$ is $\varepsilon \approx c|{\bf p}|$ and, in our case, $|{\bf p}| \approx p_{\parallel}$. If the electron experiences a significant momentum gain, then the terminal longitudinal electron momentum is $p_{\parallel}^{term} \approx \Delta p_{\parallel}^{term}$. Putting all these estimates together, we find that the terminal electron energy is given by $\varepsilon^{term} \approx c \Delta p_{\parallel}^{term}$. For modes with an even p index, the momentum gain is given by equation (37). We also take into account the relation between a_{\parallel} and P given by equation (28). As a result we arrive to the following expression for the electron energy gain:

$$\varepsilon^{term}[\text{GeV}] \approx \frac{0.72}{p+1}\cos(\Phi_0 - \pi)P^{1/2}[\text{PW}]. \tag{38}$$

The result is independent of the spot size w_0 and wavelength λ_0 . At the end of section 3, we examined the field structure of a circularly-polarized 0.6 PW laser beam with l=-1, $\sigma=1$, and p=0. According to equation (38), we expect this beam to generate electrons with hundreds of MeV in energy, since $\varepsilon^{term} \approx 0.56 \cos(\Phi_0 - \pi)$ GeV.

4. Simulation results for a normally incident 600 TW laser

In section 3, we provided preliminary estimates showing that a properly chosen beam with twisted wavefronts can generate forward-directed ultra-relativistic electrons. In this section, we present a self-consistent analysis, performed using a 3D

Table 1. 3D PIC simulation parameters.

Laser parameters	
Peak power (period averaged)	0.6 PW
Twist and radial index	l = -1, p = 0
Right-circular polarization	$\sigma = 1$
Wavelength	$\lambda_0 = 0.8 \; \mu \mathrm{m}$
Pulse duration (sin ²	$\tau_g = 20 \text{ fs}$
electric field)	
Focal spot size (1/e	$w_0 = 3 \mu \text{m}$
electric field)	
Location of the focal plane	$x = 0 \mu m$
Direction of the incident	-x
laser	

Other parameters

Position of the bulk target	$-1.0 \ \mu \text{m} \le x \le -0.3 \ \mu \text{m}$
Position of the	$-0.3 \ \mu \text{m} < x \le 0.0 \ \mu \text{m}$
pre-plasma	
Electron and C ⁺⁶ density	$n_e = 500 n_c$ and $n_{Carbon} = 83.3 n_c$
Gradient length	$L = \lambda_0/20$
Simulation box $(x \times y \times z)$	$10 \ \mu \text{m} \times 30 \ \mu \text{m} \times 30 \ \mu \text{m}$
Moving window start time	11 fs
Moving window velocity	c
Cell number $(x \times y \times z)$	$400 \text{ cells} \times 800 \text{ cells} \times 800 \text{ cells}$
Macroparticles per cell for	300 at $r < 2.5 \mu m$, 36 at $r > 2.5 \mu m$
electrons	
Macroparticles per cell for	24
C^{+6}	

PIC simulation, of electron injection and subsequent acceleration by a laser beam with dominant E_{\parallel} and B_{\parallel} in the near-axis region.

In our simulation, a 600 TW circularly-polarized Laguerre-Gaussian beam with l = -1, $\sigma = 1$, and p = 0 is normally incident on a mirror that is initialized as a fully ionized plasma with a sharp density gradient. The incident pulse propagates in the negative direction along the x-axis. The laser envelope function $g(\xi)$ has a temporal profile such that $g(t) = \sin^2(0.5\pi * t/\tau_g)$ with a total duration of $\tau_g = 20$ fs. The beam width is $w_0 = 3$ µm, the laser wavelength is $\lambda_0 =$ 0.8 μ m, and the focal plane is located at $x = 0 \mu$ m. The mirror is a carbon plasma with an electron density profile $n_e = 500 n_c \exp[-20(x + 0.3 \ \mu m)/\lambda_0]$ at $x \ge -0.3 \ \mu m$, where $n_c = 1.8 \times 10^{27} \ m^{-3}$ is the critical density for $\lambda_0 = 0.8 \ \mu m$. While ion mobility does not appear to affect the simulation results, the ions are left mobile so as to ensure a more realistic scenario. The initial kinetic energy of all particles (electrons and ions) is set to zero. In order to follow the electrons bunches over a long period of time a moving window is employed. The window size is set to encompass the entire simulation box and moves at a velocity c, beginning at a time t = 11 fs. Additional simulation details are provided in table 1.

The field structure of the incident laser beam in the (x, z)-plane is shown in figure 4. The time snapshots are taken at t = -9 fs. We define t = 0 as the time when, in the absence of the mirror, the peak of the laser envelope reaches at x = 0. As can be seen in figure 4, the longitudinal fields E_x and B_x are

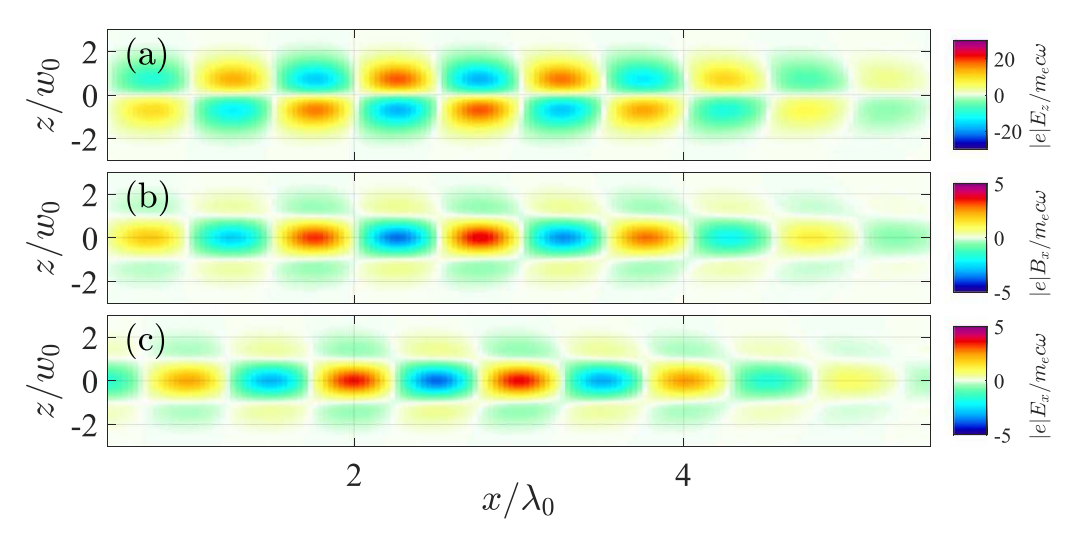


Figure 4. Field structure of an incident circularly-polarized Laguerre–Gaussian laser beam from a 3D PIC simulation. The snapshots are taken at t = -9 fs. The laser beam and simulation parameters are given in table 1.

strongest on-axis where the transverse field E_z tends to zero. The field structure in these snapshots agrees with the paraxial analysis presented in section 2 for beams with twisted wavefronts.

The laser-plasma interaction that occurs after the laser reaches the mirror can be sorted into two stages: the injection stage and the acceleration stage. The injection stage occurs during laser reflection off the plasma mirror. At this stage, plasma electrons are drawn out of the mirror by laser fields and injected into the near-axis region of the laser beam in front of the mirror. The electron injections stops after the laser beam is fully reflected off the mirror. Results from tracking the particles in the third bunch back to the target surface show a complex relationship between the transverse and longitudinal field structures. This process requires significant further research that is beyond the scope of this article. During the acceleration stage, the injected electrons travel with the reflected laser beam away from the surface of the mirror. Their longitudinal motion is caused by E_{\parallel} of the reflected laser beam. Only those electrons that are injected into a region with E_{\parallel} < 0 can accelerate while moving away from the mirror. On the other hand, no acceleration is possible when $E_{\parallel} > 0$ in the vicinity of the mirror surface. As a result, oscillations of $E_{\parallel} > 0$ near the mirror surface generate electron bunches rather than a continuous electron beam. The maximum areal density of a bunch, ρ_e , (integral of n_e along the bunch) can be estimated by taking into account that the injection process during one laser period stops once the space-charge of the extracted electrons shields E_{\parallel} of the laser. This yields $\rho_e \approx a_{\parallel} n_c c / \omega$

$$\rho_e[\text{m}^{-2}] \approx 1.3 \times 10^{22} P^{1/2} \text{ [PW] } \lambda_0 \text{ [}\mu\text{m] } w^{-2} \text{ [}\mu\text{m]}.$$
 (39)

The implication is that a beam with a strong longitudinal electric field is expected to produce high density bunches.

Figure 5(a) shows that the accelerated electrons indeed travel in bunches. The snapshot is taken at t = 261 fs after the injected electrons have traveled roughly 100 λ_0 along the x

axis with the laser beam. The plot shows the distribution of the electrons located in the region near the axis with $r < 1.5 \mu m$ in the (ε_e, x) -space. The compactness of the bunches, both in transverse (see figure 6(c)) and longitudinal directions (see figure 5(a)), ensures that the electrons in each bunch essentially experience the same accelerating field. This explains the narrow energy spread within each bunch in figure 5(a).

The evolution of the energy spectrum within a single bunch is plotted in figure 5(c). The selected bunch is marked as bunch #3 in figure 5(a). The bunch retains a relatively narrow energy spread during the acceleration process. The dashed curve shows the prediction given by equation (36) for an injection phase of $\Phi_0=0.8\pi$. The good agreement indicates that the accelerated electrons are likely injected into the same phase of the reflected beam. There is also a strong correlation between electrons which have a high energy and those with a low divergence angle. This is best seen in figure 5(d) which shows the distribution of energy versus divergence angle $\theta=\arctan(p_\perp/p_\parallel)$ of the third bunch.

The presented simulation demonstrates that a normally incident 600 TW beam can generate several dense bunches of ultra-relativistic electrons. Specifically, the terminal energy of the electrons in the third bunch is 0.47 GeV with a FWHM of $\sim 10\%$ (see figure 5(b) for a snapshot at t = 261 fs). The bunch has a duration of roughly 400 as and a total electron charge of 26 pC, while the normalized transverse emittance is 9.5 μ m.

5. The impact of the longitudinal magnetic field on electron dynamics

The most distinctive feature of the considered laser beam with twisted wavefronts is the strong longitudinal magnetic field B_{\parallel} in the near-axis region. In what follows, we examine the profound impact of this field on electron dynamics.

In addition to E_{\parallel} , the electrons in the near-axis region experience B_{\parallel} that can provide transverse confinement at an early stage of the acceleration before the electron momentum becomes predominantly forward-directed. The importance of

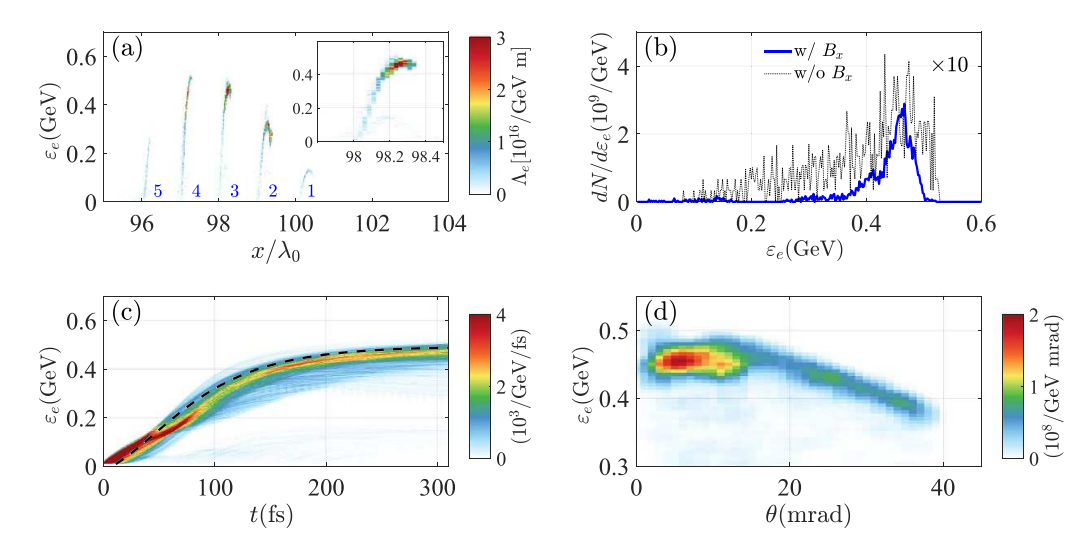


Figure 5. (a) Accelerated electron bunches at t = 261 fs. The color shows the distribution of electrons with r < 1.5 μm in the (ε_e, x) -space. The inset shows the structure of the third bunch. (b) The energy spectrum $dN/d\varepsilon_e$ in the third bunch at t = 261 fs for electrons with r < 1.5 μm for cases with (blue line) or without (black line, multiplied by 10 to aid the comparison) the force from B_x in the electron equation of motion. (c) The time evolution of the energy spectrum of the third bunch. The black dashed curve is the prediction of equation (36) with $\Phi_0 = 0.8\pi$. (d) The energy-angle distribution in the third bunch at t = 261 fs.

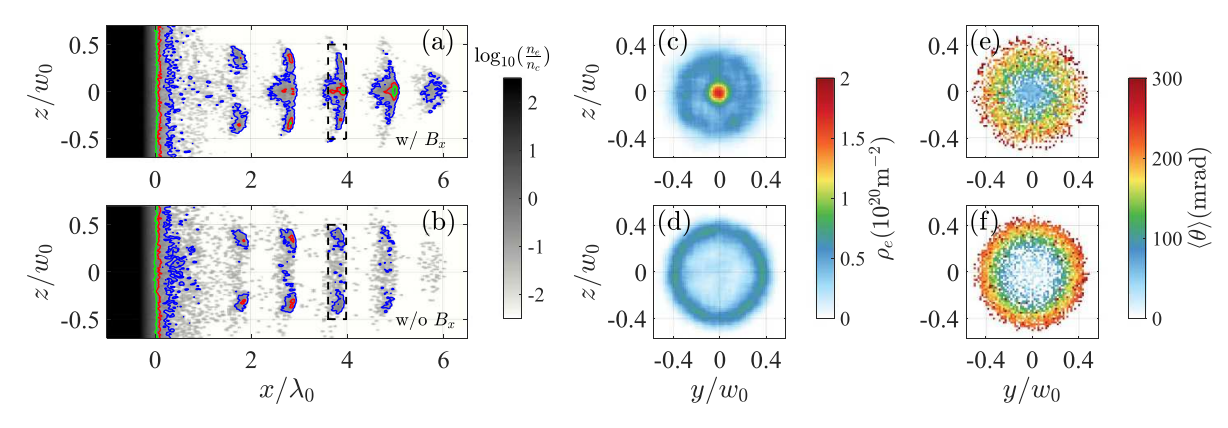


Figure 6. A comparison between 3D PIC simulations with (upper row) and without B_x (bottom row) in the electron equations of motion. Both simulations use the same 600 TW laser beam with parameters given in table 1. All snapshots are taken at t = 9 fs. (a), (b): Electron density on a log-scale, with the color representing $\log(n_e/n_c)$. The blue, red, and green contours denote $n_e = 0.1n_c$, 0.5 n_c , and n_c . The dashed rectangle shows the radial and longitudinal extent of what is referred to as the third bunch in the remaining panels. (c), (d): Areal density of the electrons in the third bunch. (e), (f): Cell-averaged electron divergence angle $\langle \theta \rangle$ in the third bunch. The angle $\theta \equiv \arctan(p_\perp/p_x)$ of an individual electron is averaged over the electrons located within the cells with the same y and z coordinates.

 B_{\parallel} can be assessed by estimating the Larmor radius, r_L , for an electron injected with transverse relativistic momentum p_{\perp} into the field near the focal plane, whose strength is given by equation (28). We find that

$$r_L/w_0 \approx \frac{2.2 \times 10^{-3}}{\sqrt{1+p}} \left(\frac{p_{\perp}}{m_e c}\right) \left(\frac{w_0}{\lambda_0}\right) P^{-1/2} [PW].$$
 (40)

In the case of the 600 TW laser beam considered in section 4, we have $r_L/w_0 \approx 10^{-2} p_\perp/m_e c$. Even for those electrons that are injected with $p_\perp/m_e c \approx |e|E_\perp^{\rm max}/m_e c\omega \approx 19$, the Larmor radius, $r_L \approx 0.2~w_0$, is significantly smaller than the beam waist. By keeping the injected electrons close to the axis, B_\parallel ensures that the electrons are unable to sample strong E_\perp and gain additional transverse momentum. As a result, they are predominantly accelerated by E_\parallel , which leads to a strongly

collimated beam. It is important to point out that B_{\parallel} is shifted by $\pi/2$ with respect to E_{\parallel} , which means that the direction of the electron rotation induced by the magnetic field changes during the acceleration process.

At the injection stage, plasma electrons experience a complicated interplay of transverse and longitudinal fields that is not captured by the presented estimate. The impact of B_x during this process can be elucidated by removing its effects from the electron dynamics even though this does lead to a somewhat non-physical scenario. To remove the effect of B_x in the PIC simulation, we multiply the B_x variable by zero in the relevant section of the particle pusher. Figure 6(b) shows the electron density obtained using this approach for the laser-mirror interaction examined in section 4. For comparison, figure 6(a) also shows the electron density from the original simulation where the effect of B_x is included. The bunches in figure 6(b)

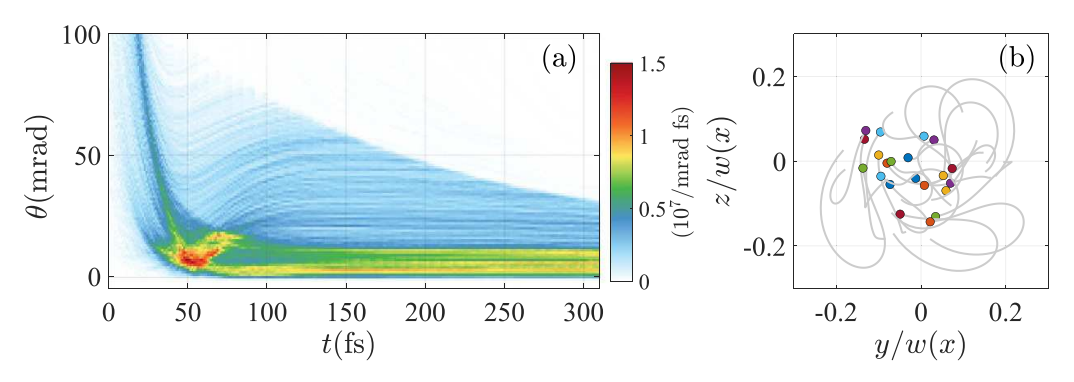


Figure 7. (a) Time evolution of the electron distribution over the divergence angle θ in the third bunch ($r < 1.5 \mu m$). (b) Trajectories of electrons randomly chosen from the third bunch at t = 261 fs. The trajectories correspond to 6 fs $\leq t \leq 261$ fs, with the circles marking the electron positions at t = 261 fs. The transverse coordinates are normalized to the local width of the laser beam $w(x) = w_0 \sqrt{1 + x^2/x_R^2}$.

form in a ring-like structure *away* from the central axis. The structure of the bunches appears superficially similar to that observed for radially polarized beams at lower intensities [9]. In contrast to that, the electron bunches in figure 6(a) are formed close to the axis in the region where the longitudinal field dominates. The bunches become more compact as they move away from the mirror, with the electron density exceeding n_c .

Figures 6(c)–(f) compare the areal density and divergence angle between the two simulations. The comparison is performed for the electrons within the third bunch in figures 6(a) and (b). The radial and longitudinal extend of the third bunch is shown with the the black dashed rectangles in figures 6(a) and (b). The difference in collimation is striking even at this injection stage (t = 9 fs). The higher areal density point-like structure seen in figure 6(c) is complimented by a corresponding small cell-averaged electron divergence angle $\langle \theta \rangle$ seen in figure 6(e). The averaging, indicated by the angular brackets, is performed by taking all the electrons located within the cells with the same y and z coordinates, i.e. the cells with the same projection onto the transverse plane. The averaging accounts for the difference in the numerical weight w_{α} of individual macro-particles caused by the initial density gradient: $\langle \theta \rangle = \sum_{\alpha} w_{\alpha} \theta_{\alpha} / \sum_{\alpha} w_{\alpha}$. In the case where the influence of B_x is removed (with the corresponding plots of areal density in figure 6(d), and cell-averaged divergence in figure 6(f), we see a ring-like 'bunch' with divergent profile indicating that it will continue to diverge long after the injection stage is over. The contrasting pictures between the two simulations show the important role of the B_x .

Figure 5(b) shows the energy spectrum of the third bunch in the simulation without the B_x forces at a much later time (t = 261 fs). The same figure shows the spectrum for the third bunch in the original simulation at the same time instant. Both spectra are calculated for the electrons in the near-axis region with r < 1.5 µm. Not surprisingly, the electrons moving close to the central axis achieve similar energies in both simulations. However, the number of such energetic electrons in the simulation without the B_x forces is an order of magnitude lower. During the injection process and at the very early acceleration stage the longitudinal magnetic field provides a significant amount of transverse electron confinement. This keeps

electrons in the region with a strong E_x but weak E_{\perp} , which ensures good collimation of the electron bunches.

To further examine the transverse electron motion during the acceleration process, we have tracked several electrons. The electrons are randomly selected from the third bunch $(r < 1.5 \mu m)$ at t = 261 fs. The projection of the electron trajectories onto the transverse plane for 6 fs $\leq t \leq$ 261 fs is shown in figure 7(b), where the circles indicate the electron positions at t = 261 fs. The transverse coordinates are intentionally normalized to the local width of the laser beam $w(x) = w_0 \sqrt{1 + x^2/x_R^2}$ to correlate the electron location with the strength of the transverse electric field E_{\perp} that increases away from the central axis. As expected, there is a pronounced rotation induced by B_{\parallel} that prevents electrons from expanding and reaching a region with a strong E_{\perp} . This rotation is also observed to reverse, effectively twisting the trajectory of the electrons. This feature is caused by the $\pi/2$ shift between E_{\parallel} and B_{\parallel} . The sign of B_{\parallel} changes during the acceleration process, which causes the electrons to rotate in the opposite direction and manifests itself as the twist seen in figure 7(b) for each individual trajectory.

Another important metric of the electron dynamics is the divergence angle θ . Figure 7(a) shows how the electron distribution over $\theta = \arctan\left(p_\perp/p_\parallel\right)$ changes with time in the third bunch. We find that the bunch becomes less divergent over time, which is a clear indicator of the dominant role played by E_\parallel . Indeed, θ decreases because p_\parallel increases at a much faster rate than p_\perp . The increase in p_\parallel is caused by E_\parallel , as already discussed in section 3. The changes in p_\perp are caused by E_\perp . The longitudinal magnetic field has no direct impact on the divergence angle since it rotates p_\perp without changing its amplitude. However, by keeping the electrons close to the central axis, the magnetic field prevents them from experiencing a strong E_\perp that peaks off axis and, as a result, it prevents p_\perp from increasing.

We conclude this section by presenting results for a case of oblique incidence. Experimental facilities often require that laser pulses are not shot at normal incidence onto a reflecting surface so as to avoid damage to optical systems. This was our primary motivation to examine the oblique incidence case. In our simulation, the laser beam is still incident in the negative direction along the x-axis, but the target is now titled by 25° .

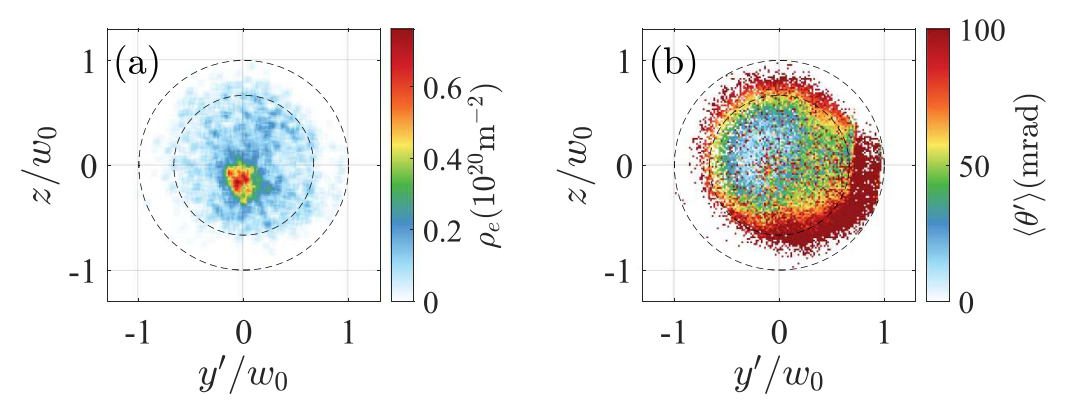


Figure 8. 3D PIC simulation results for a 25° incidence angle. The snapshots are take at t = 52 fs and plotted in an (x', y', z) system of coordinates whose x'-axis points in the specular direction. (a) Areal electron density in a third bunch moving in the specular direction. (b) Cell-averaged electron divergence angle $\langle \theta' \rangle$ in the third bunch. The angle $\theta' \equiv \arctan\left(\sqrt{p_{y'}^2 + p_z^2} / p_{x'}\right)$ is averaged on every mesh cell of the (y', z) plane.

In order to make the simulation manageable, we perform it in a window moving along the *x*-axis. The simulation time is limited compared to the case of normal incidence, because the electron bunches, that now travel at an angle to the *x*-axis, leave the simulation window prematurely. This setup does not allow enough time for the acceleration process to reach a plateau as in the normal incidence case and so the final distribution function is left for future research. Despite this limitation this simulation will allow testing the early time conditions that set up the acceleration process and bunch formation.

We find that the laser reflection again generates a series of dense collimated bunches, which indicates the robustness of the considered approach to electron acceleration. The areal density ρ_e and the cell-averaged divergence angle $\langle \theta' \rangle$ in the third bunch are shown in figures 8(a) and (b). These snapshots are taken at t=52 fs. We use an orthogonal (x',y',z) system of coordinates whose x'-axis points in the specular direction. The divergence angle $\theta' \equiv \arctan\left(\sqrt{p_{y'}^2 + p_z^2} \middle/ p_{x'}\right)$ is the angle between the momentum vector \boldsymbol{p} and the x'-axis. Even though the axial symmetry is broken, there is still strong evidence of a dense non-divergent bunch close to the laser axis. The high degree of collimation following the injection suggests that the reflected laser pulse would generate highly energetic bunches with similar characteristics to the case presented at normal incidence.

6. Summary and discussion

In summary, this manuscript presents a detailed analysis of the topology of linearly and circularly polarized Laguerre–Gaussian laser beams. It is shown that the beams with a twist index |l|=1 have a distinct field structure in the near-axis region with dominant E_{\parallel} and B_{\parallel} . In the case of circularly polarized beams, the rotation of E_{\perp} should be in the opposite direction to the rotation of the wavefronts, i.e. $\sigma=-l$, to achieve such a structure. The manuscript also presents kinetic 3D PIC simulations for a 600 TW circularly polarized beam $(p=0, l=-1, \text{ and } \sigma=1)$ reflected off a plasma

mirror. The dominant E_{\parallel} and B_{\parallel} combine to inject dense electron bunches upon reflection. The bunches are effectively accelerated by E_{\parallel} while being confined by B_{\parallel} . The magnetic field prevents the bunch electrons from traveling too far radially outwards, so they sample a relatively weak transverse electric field and remain well-collimated. The bunch with the largest energy has a distinctly narrow energy spread with a FWHM of just 10%. The terminal energy gain for an individual bunch is well predicted by the analytical model developed in the manuscript. The charge of a single bunch in the simulation is as high as 26 pC. The bunches have a duration of \sim 400 as and a remarkably low divergence of just 1.15° (20 mrad).

The nearest analogue to the discussed mechanism is the acceleration by a radially polarized laser beam. Such a beam also has a strong longitudinal electric field that dominates the field structure in the region close to the central axis. However, in contrast to the beams considered in this manuscript, the radially polarized beam lacks a strong longitudinal magnetic field in the region close to the axis. As shown in appendix, the absence of B_{\parallel} has a profound impact on the electron acceleration even though the amplitude of E_{\parallel} is the same as in the case of the radially polarized beam considered in section 4. In the absence of B_{\parallel} , there is no mechanism confining electrons in the region with $r/w(x) \ll 1$. The lack of confinement also manifests itself in the case of oblique incidence. We have shown some results that indicate the robustness of the electron injection by a beam with a strong B_{\parallel} . In contrast to that, the injection by radially polarized beams is not as robust [30], which makes experimental implementation extremely challenging.

The transverse fields do have a role where they are, inpart, responsible for detaching electrons from the pre-plasma. The exact dynamical process relating to the transverse fields is likely of less importance than that of the longitudinal fields. Previous studies have discussed the ponderomotive force as a mechanism for keeping electrons [31] (and ions [32]) within the central region of the beam. However, as can be seen in the comparison made in figure 6, this does not appear to be the dominant mechanism confining the electrons close to the axis in our case, at least at early times.

While this study is limited to a relatively short laser pulse with three peaks at high amplitude, a TiSaphire laser with a FWHM of around 30 fs will have a train of roughly 15 peaks. The energy of each bunch is strongly tied to the amplitude at the position in the envelope. After being injected, electrons are accelerated directly by laser field in vacuum, implying that they are not likely subjected to instabilities that occur in bulk plasmas. The density of the bunches is also related to the longitudinal field, with higher densities recorded with higher amplitudes [28]

Using the scheme detailed in the manuscript, it may be possible to construct a source of highly collimated dense attosecond bunches of ultra-relativistic electrons suitable for potential applications. This can be achieved using a combination of high-power laser systems, similar to those already in use today. In addition to this, optical techniques that have already been put to experimental use can be used to create twisted wave-fronts necessary for this mechanism. Given the research presented here, with some further studies, a working design for a small-scale high-energy electron accelerator may be within grasping distance.

Data availability statement

The datasets generated during and analyzed during the current study are available from the corresponding author on reasonable request.

Code availability

PIC simulations were performed with the fully relativistic open-access 3D PIC code EPOCH [33].

Acknowledgments

Y S acknowledges the support by Strategic Priority Research Program of Chinese Academy of Sciences (Grant No. XDA25010200) and Newton International Fellows Alumni follow-on funding. D R B and A A acknowledge the support by the National Science Foundation (Grant No. PHY 1903098). Simulations were performed with EPOCH (developed under UK EPSRC Grants EP/G054950/1, EP/G056803/1, EP/G055165/1 and EP/ M022463/1). The simulations and numerical calculations in this paper have been done on the supercomputing system in the Supercomputing Center of University of Science and Technology of China. This work also used the Extreme Science and Engineering Discovery Environment (XSEDE), which is supported by National Science Foundation Grant Number ACI-1548562.

Appendix. 3D PIC simulation results for electron acceleration by a radially polarized laser beam

The acceleration scheme presented in this manuscript is superficially similar to that associated with radially polarized beams [9, 30]. Near the axis, radially polarized beams also have a strong longitudinal electric field, so a comparison of the two schemes is worth discussing.

The difference in the field topology can be illustrated by constructing a radially polarized beam using two circularly-polarized Laguerre–Gaussian beams from section 2: the first with l=1, $\sigma=-1$ and the second, a mirror image of the first, with l=-1, $\sigma=1$. We set $E_0=E_*/2$ for each of the beams in equation (8) that describes the structure of E_y . The resulting beam structure will be compared to a circularly polarized beam with $E_0=E_*$ and l=-1, $\sigma=1$, and p=0. The superposition of the two beams has

$$E_{y} = \frac{1}{2} E_{*} \left(e^{i\phi} + e^{-i\phi} \right) D = E_{*} \cos \phi D,$$
 (41)

where $D(\widetilde{x},\widetilde{r},\xi)=g(\xi)\exp(i\xi)\psi_{p,\pm 1}(\widetilde{x},\widetilde{r},\phi)\exp(\mp i\phi)$ is a function that, for compactness, incorporates all the remaining dependencies besides the dependence on ϕ . We next take into account that $E_z=i\sigma E_y$ in each of the circularly-polarized beams and find that the superposition of the two beams has

$$E_z = \frac{1}{2} E_* \left(-ie^{i\phi} + ie^{-i\phi} \right) D = E_* \sin \phi D.$$
 (42)

These E_z and E_v represent a radially polarized laser beam:

$$\boldsymbol{E}_{\perp} = \boldsymbol{e}_r E_* D. \tag{43}$$

In the context of the electron acceleration mechanism, the biggest difference between the radially polarized beam and the circularly polarized beam with twisted wavefronts is the absence of B_{\parallel} near the axis. In order to find the structure of the longitudinal fields, we use equations (19) and (20). Close to the axis, the longitudinal electric fields of the two beams are the same, so the longitudinal field of the radially polarized beam is given by

$$E_{x} = \frac{i\theta_{d}}{2} \frac{1}{\widetilde{r}} e^{-i\phi} \left[\frac{E_{*}}{2} e^{i\phi} \right] + \frac{i\theta_{d}}{2} \frac{1}{\widetilde{r}} e^{i\phi} \left[\frac{E_{*}}{2} e^{-i\phi} \right] = \frac{i\theta_{d}}{2} \frac{1}{\widetilde{r}} E_{*}. \tag{44}$$

It follows directly from equation (19) that it is equal to E_x of the circularly polarized beam with $E_0 = E_*$ and l = -1, $\sigma = 1$, and p = 0 that we are using for our comparison. On the other hand, the longitudinal magnetic fields of the two circularly-polarized beams cancel each other out, so that there is no strong B_x close to the axis of the resulting radially polarized beam:

$$B_{x} = -\frac{\theta_{d}}{2} \frac{1}{\widetilde{r}} e^{-i\phi} \left[\frac{E_{*}}{2} e^{i\phi} \right] + \frac{\theta_{d}}{2} \frac{1}{\widetilde{r}} e^{i\phi} \left[\frac{E_{*}}{2} e^{-i\phi} \right] = 0. \quad (45)$$

In contrast to this, B_x of the circularly polarized beam with l = -1 and $\sigma = 1$ that we use for our comparison has the same amplitude as E_x .

Even though E_x has the same amplitude in the two beams that are being compared, the power in the radially polarized beam is two times lower. In order calculate the power of the radially polarized beam, we note that $B_z = E_y$ and $B_y = -E_z$.

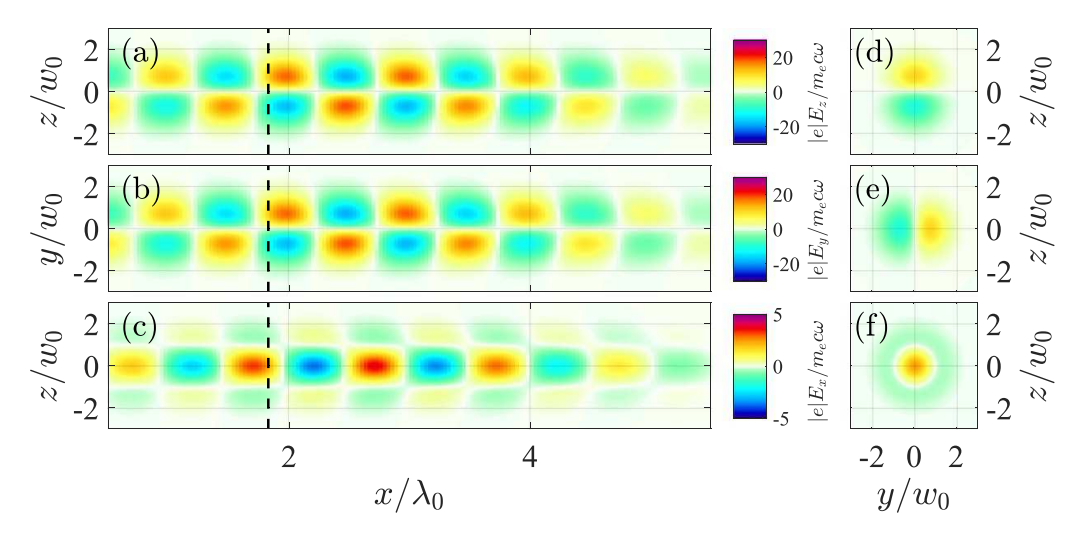


Figure 9. Electric field components of a radially polarized laser beam *before* it encounters the mirror. Panels (a) and (d) show E_z ; panels (b) and (e) show E_y ; panels (c) and (f) show E_x . The left column ((a)–(c)) shows the field structure in the (x, z)-plane at y = 0. The right column ((d)–(f)) shows the field structure in the (y, z)-plane at the x-position indicated with the dashed line. All the snapshots are taken a time $t \approx -9$ fs.

The longitudinal component of the Poynting vector is then given by

$$S_x = \frac{c}{4\pi} \left[(\text{Re}E_y)^2 + (\text{Re}E_z)^2 \right] = \frac{c}{4\pi} E_*^2 (\text{Re}D)^2.$$
 (46)

The peak period-averaged power is

$$P_{rad} = \left\langle \int_{0}^{2\pi} d\phi \int_{0}^{\infty} S_{x} r dr \right\rangle$$
$$= \frac{cw_{0}^{2}}{4\pi} \int_{0}^{2\pi} d\phi \int_{0}^{\infty} \left\langle (\text{Re}D)^{2} \right\rangle \widetilde{r} d\widetilde{r} \tag{47}$$

with $g(\xi) = 1$. After time-averaging, the expression on the right-hand side is identical to the expression on the right-hand side of equation (15). Thus the peak period-averaged power of the radially polarized beam is

$$P_{rad} = \frac{cw_0^2}{8\pi} E_0^2. \tag{48}$$

Not that it is equal to P_{lin} , the power of a linearly polarized beam with $E_0 = E_*$, given by equation (16). On the other hand, the peak period-averaged power of a circularly polarized beam, P_{CP} , with $E_0 = E_*$, l = -1, $\sigma = 1$, and p = 0 is $2P_{lin}$, where P_{lin} is given by equation (16). We thus have

$$P_{CP} = \frac{cw_0^2}{4\pi} E_0^2 = 2P_{rad}.$$
 (49)

If both types of beams can be generated at the same power, then a potential advantage of using the radially polarized beam would be its ability to generate higher E_{\parallel} . However, very different optical techniques are employed to generate the two types of beams. The radially polarized beams are produced using transmissive optical elements, which limits the incident power. In contrast to that, the beams with twisted wavefronts can be produced by adding an etched mirror [13, 25] at some

point into a traditional laser-system. This method relies of laser reflection, so it does not have the same power limitation. This means that it can potentially be used to generate the desired beams at very high power and reach very strong E_{\parallel} .

To compare the acceleration by the two beams with the same strength of E_{\parallel} , we performed an additional simulation for a 300 TW radially polarized beam. With the exception of the laser power, all other simulation parameters are the same as those listed in table 1 and used to obtain the results presented in section 4. The electric field structure in the (x,z)-plane at t=-9 fs is shown in figure 9. The longitudinal electric field structure in the region close to the axis is nearly identical to that shown in figure 4 for the circularly-polarized Laguerre–Gaussian beam. There is no strong B_{\parallel} near the axis, which agrees with the analytical analysis given by equations (44) and (45).

To obtain a comparable picture of the phenomena in the new simulation, we again focus on the third bunch formed during the reflection process (see figure 6 for the location of this in the circularly-polarized Laguerre–Gaussian case). The evolution of the energy spectrum of this bunch is shown for the radial polarized case in figure 10(a) whereas the energy-angle distribution is shown in figure 10(b). These plots can be compared to similar plots in figure 5. In the radially polarized case, we see a slightly lower peak kinetic energy at later times. In addition to this, the bunch has a wider energy spectrum. When looking at the energy-angle distribution, the bunch appears to be spread over a slightly wider divergence angle. The spectra in the radially-polarized case do not show the highly narrow energy spread features present in the circularly-polarized case.

Previous studies [30] have shown that the acceleration by radially polarized beams can be affected by the highharmonic radiation emitted during the reflection. To test for this sensitivity, we performed two more simulations, one for each beam scenario. In these simulations, the cell size is reduced from 25 to 20 nm and the default second order

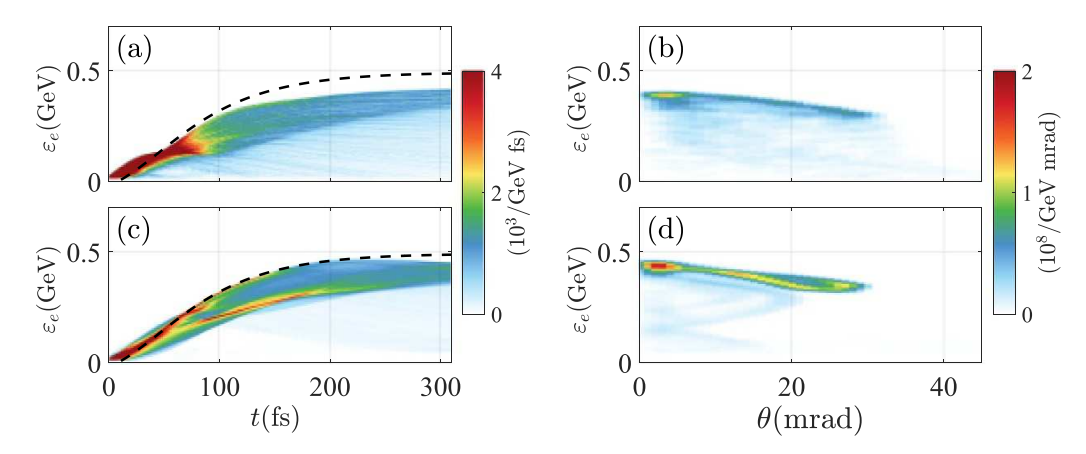


Figure 10. Sensitivity of the electron acceleration by a 300 TW radially polarized beam to simulation parameters. The top row (subplots (a) and (b)) shows results for the parameters from table 1. The bottom row (subplots (c) and (d)) shows results from a simulation with a reduced cell size of 20 nm and a higher-order field solver. The black dashed curve is prediction of equation (36) for $\Phi_0 = 0.8\pi$. The left column is the energy distribution as a function of time for the third bunch of electrons. The right column is energy-angle distribution at t = 261 fs.

Yee scheme is changed to the fourth order version. The results for the circularly-polarized Laguerre-Gaussian beam are unchanged, which is unsurprising given the extensive resolution tests previously run [28, 34]. The new results for the radially-polarized case are visibly different compared to those from the original simulation: there are differences in the maximum energy, energy spread, and the energy-angle distribution. There is also some evidence, which is not plotted here, of a series of odd harmonics forming on reflection of the beam in the radially polarized case. No such high-harmonic generation is evident in the circularly-polarized Laguerre-Gaussian case. The studies focused on radially polarized beams typically use the field solvers specifically designed for accurate propagation of high-harmonic generation [9, 30, 35]. While the results of figure 10 primarily show the sensitivity of the radially polarized mechanism to resolving the high-harmonic generation, there is experimental evidence [30] that highharmonics do have a significant impact when reflecting this type of beam at an angle away from normal off a plasma mirror.

ORCID iDs

Yin Shi https://orcid.org/0000-0001-9902-873X

David R Blackman https://orcid.org/0000-0001-7852-4216

Alexey Arefiev https://orcid.org/0000-0002-0597-0976

References

- [1] Danson C N *et al* 2019 Petawatt and exawatt class lasers worldwide *High Power Laser Sci. Eng.* 7 e54
- [2] Esarey E, Schroeder C B and Leemans W P 2009 Physics of laser-driven plasma-based electron accelerators Rev. Mod. Phys. 81 1229–85
- [3] Gibbon P 2004 Short Pulse Laser Interactions with Matter (Singapore: World Scientific Publishing Company)

- [4] Arefiev A V, Khudik V N, Robinson A P L, Shvets G, Willingale L and Schollmeier M 2016 Beyond the ponderomotive limit: direct laser acceleration of relativistic electrons in sub-critical plasmas *Phys. Plasmas* 23 056704
- [5] Stupakov G V and Zolotorev M S 2001 Ponderomotive laser acceleration and focusing in vacuum for generation of attosecond electron bunches *Phys. Rev. Lett.* 86 5274–7
- [6] Pukhov A, Sheng Z-M and Meyer-ter Vehn J 1999 Particle acceleration in relativistic laser channels *Phys. Plasmas* 6 2847–54
- [7] Willingale L et al 2011 High-power, kilojoule class laser channeling in millimeter-scale underdense plasma Phys. Rev. Lett. 106 105002
- [8] Gong Z, Mackenroth F, Wang T, Yan X Q, Toncian T and Arefiev A V 2020 Direct laser acceleration of electrons assisted by strong laser-driven azimuthal plasma magnetic fields *Phys. Rev.* E 102 013206
- [9] Zaïm N, Thévenet M, Lifschitz A and Faure J 2017 Relativistic acceleration of electrons injected by a plasma mirror into a radially polarized laser beam *Phys. Rev. Lett.* 119 094801
- [10] Sprangle P, Esarey E and Krall J 1996 Laser driven electron acceleration in vacuum, gases and plasmas *Phys. Plasmas* 3 2183–90
- [11] Shen B, Bu Z, Xu J, Xu T, Ji L, Li R and Xu Z 2018 Exploring vacuum birefringence based on a 100 PW laser and an x-ray free electron laser beam *Plasma Phys. Control. Fusion* 60 044002
- [12] Leblanc A, Denoeud A, Chopineau L, Mennerat G, Martin P and Quere F 2017 Plasma holograms for ultrahigh-intensity optics *Nat. Phys.* 13 440–3
- [13] Shi Y, Shen B, Zhang L, Zhang X, Wang W and Xu Z 2014 Light fan driven by a relativistic laser pulse *Phys. Rev. Lett.* 112 235001
- [14] Longman A and Fedosejevs R 2017 Mode conversion efficiency to Laguerre-Gaussian OAM modes using spiral phase optics *Opt. Express* 25 17382–92
- [15] Vieira J, Trines R M M, Alves E P, Fonseca R A, Mendonça J T, Bingham R, Norreys P and Silva L O 2016 High orbital angular momentum harmonic generation *Phys. Rev. Lett.* 117 265001
- [16] Zhang X, Shen B, Shi Y, Wang X, Zhang L, Wang W, Xu J, Yi L and Xu Z 2015 Generation of intense high-order vortex harmonics *Phys. Rev. Lett.* 114 173901
- [17] Vieira J, Mendonça J T and Quéré F 2018 Optical control of the topology of laser-plasma accelerators *Phys. Rev. Lett.* 121 054801

- [18] Shi Y, Vieira J, Trines R M G M, Bingham R, Shen B F and Kingham R J 2018 Magnetic field generation in plasma waves driven by copropagating intense twisted lasers *Phys. Rev. Lett.* 121 145002
- [19] Ju L B, Zhou C T, Jiang K, Huang T W, Zhang H, Cai T X, Cao J M, Qiao B and Ruan S C 2018 Manipulating the topological structure of ultrarelativistic electron beams using Laguerre–Gaussian laser pulse *New J. Phys.* 20 063004
- [20] Zhu X-L, Chen M, Weng S-M, McKenna P, Sheng Z-M and Zhang J 2019 Single-cycle terawatt twisted-light pulses at midinfrared wavelengths above 10 μm Phys. Rev. Appl. 12 054024
- [21] Tikhonchuk V, Korneev P, Dmitriev E and Nuter R 2020 Numerical study of momentum and energy transfer in the interaction of a laser pulse carrying orbital angular momentum with electrons *High Energy Density Phys*. 37 100863
- [22] Nuter R, Korneev P, Thiele I and Tikhonchuk V 2018 Plasma solenoid driven by a laser beam carrying an orbital angular momentum *Phys. Rev.* E 98 033211
- [23] Blackman D R, Nuter R, Korneev P and Tikhonchuk V T 2020 Nonlinear landau damping of plasma waves with orbital angular momentum *Phys. Rev.* E 102 033208
- [24] Denoeud A, Chopineau L, Leblanc A and Quéré F 2017 Interaction of ultraintense laser vortices with plasma mirrors *Phys. Rev. Lett.* 118 033902
- [25] Longman A, Salgado C, Zeraouli G, naniz J I A, Pérez-Hernández J A, Eltahlawy M K, Volpe L and Fedosejevs R 2020 Off-axis spiral phase mirrors for generating high-intensity optical vortices *Opt. Lett.* 45 2187–90
- [26] Bae J Y *et al* 2020 Generation of low-order Laguerre-Gaussian beams using hybrid-machined reflective spiral phase plates

- for intense laser-plasma interactions *Results Phys.* **19** 103499
- [27] Aboushelbaya R et al 2020 Measuring the orbital angular momentum of high-power laser pulses Phys. Plasmas 27 053107
- [28] Shi Y, Blackman D, Stutman D and Arefiev A 2021 Generation of ultrarelativistic monoenergetic electron bunches via a synergistic interaction of longitudinal electric and magnetic fields of a twisted laser *Phys. Rev. Lett.* 126 234801
- [29] Allen L, Beijersbergen M W, Spreeuw R J C and Woerdman J P 1992 Orbital angular momentum of light and the transformation of Laguerre-Gaussian laser modes *Phys.* Rev. A 45 8185–9
- [30] Zaïm N, Guénot D, Chopineau L, Denoeud A, Lundh O, Vincenti H, Quéré F and Faure J 2020 Interaction of ultraintense radially-polarized laser pulses with plasma mirrors *Phys. Rev. X* 10 041064
- [31] Jiang C, Wang W P, Weber S, Dong H, Leng Y X, Li R X and Xu Z Z 2021 *High Power Laser Sci. Eng.* **9** e44
- [32] Pae K H, Song H, Ryu C-M, Nam C H and Kim C M 2020 Low-divergence relativistic proton jet from a thin solid target driven by an ultra-intense circularly polarized Laguerre–Gaussian laser pulse *Plasma Phys. Control.* Fusion 62 055009
- [33] EPOCH Particle-In-Cell code for plasma simulations (available at: https://github.com/epochpic/epochpic. github.io) (Accessed 20 October 2021)
- [34] Derouillat J *et al* 2018 Smilei: a collaborative, open-source, multi-purpose particle-in-cell code for plasma simulation *Comput. Phys. Commun.* 222 351–73
- [35] Chopineau L et al 2019 Identification of coupling mechanisms between ultraintense laser light and dense plasmas Phys. Rev. X 9 011050